Research Paper

Tumor-triggered drug release from calcium carbonate-encapsulated gold nanostars for near-infrared photodynamic/photothermal combination antitumor therapy

Yanlei Liu[1, 2], Xiao Zhi[1], Meng Yang[1], Jingpu Zhang[2], Lingnan Lin[3], Xin Zhao[5], Wenxiu Hou[1], Chunlei Zhang[1], Qian Zhang[1], Fei Pan[1, 4], Gabriel Alfranca[1], Yuming Yang[1], Jesús M. de la Fuente[1], Jian Ni[1], Daxiang Cui[1, 4]✉

1. Institute of Nano Biomedicine and Engineering, Key Laboratory for Thin Film and Micro fabrication of the Ministry of Education, Department of Instrument Science and Engineering, School of Electronic Information and Electrical Engineering, Shanghai Jiao Tong University, 800 Dongchuan Road, Shanghai 200240, P. R. China;
2. School of Biomedical Engineering, Shanghai Jiao Tong University, 800 Dongchuan Road, Shanghai 200240, P. R. China;
3. Institute of Refrigeration and Cryogenics, Shanghai Jiao Tong University, 800 Dongchuan Road, Shanghai 200240, P. R. China;
4. National Center for Translational Medicine, Shanghai Jiao Tong University, 800 Dongchuan Road, Shanghai 200240, P. R. China;
5. School of Life Science and Technology, Xi'an Jiaotong University, 28 Xianning Xi Road, Shanxi 710049, P. R. China.

✉ Corresponding author: Tel: 0086-21-34206886; Fax: 0086-21-34206886; E-mail: dxcui@sjtu.edu.cn

Abstract

Different stimulus including pH, light and temperature have been used for controlled drug release to prevent drug inactivation and minimize side-effects. Herein a novel nano-platform (GNS@CaCO$_3$/ICG) consisting of calcium carbonate-encapsulated gold nanostars loaded with ICG was established to couple the photothermal properties of gold nanostars (GNSs) and the photodynamic properties of indocyanine green (ICG) in the photodynamic/photothermal combination therapy (PDT/PTT). In this study, the calcium carbonate worked not only a drug keeper to entrap ICG on the surface of GNSs in the form of a stable aggregate which was protected from blood clearance, but also as the a pH-responder to achieve highly effective tumor-triggered drug release locally. The application of GNS@CaCO$_3$/ICG for *in vitro* and *in vivo* therapy achieved the combined antitumor effects upon the NIR irradiation, which was superior to the single PDT or PTT. Meanwhile, the distinct pH-triggered drug release performance of GNS@CaCO$_3$/ICG implemented the tumor-targeted NIR fluorescence imaging. In addition, we monitored the bio-distribution and excretion pathway of GNS@CaCO$_3$/ICG based on the NIR fluorescence from ICG and two-photon fluorescence and photoacoustic signal from GNSs, and the results proved that GNS@CaCO$_3$/ICG had a great ability for tumor-specific and tumor-triggered drug release. We therefore conclude that the GNS@CaCO$_3$/ICG holds great promise for clinical applications in anti-tumor therapy with tumor imaging or drug tracing.

Key words: Calcium carbonate; Gold nanostars; Tumor-triggered; Combination antitumor therapy.

Introduction

With the invention and development of laser technology, photo-based therapeutic modalities such as photodynamic therapy (PDT) and photothermal therapy (PTT) have become prospective minimally invasive approaches for cancer treatment [1-5]. PDT uses photosensitizers exposed to a laser tuned to a specific wavelength to produce highly reactive oxygen species, especially singlet oxygen ($^1O_2$), finally leading to the death of malignant cells [6-8], while photothermal therapy causes hyperthemia in tissues when absorbing energy from a laser [9-10]. The primary challenge of the photo-based anti-cancer

therapy is to define a method that ensures the specific killing effect of malignant tissues, while minimizing the side-effect to normal tissues or organs. A proper selection of photo-active materials and irradiation conditions should be addressed. Due to the low intrinsic scattering and absorption from soft tissues, the near-infrared light (NIR, 700-1100 nm) region is considered as an interesting biological window to achieve specific treatments. As for PDT, tricarbocyanine dye indocyanine green (ICG) is approved as prospective NIR photosensitizer by the US Food and Drug Administration for clinical imaging and diagnosis [6, 11-12]. However, ICG has some intrinsic drawbacks, such as poor stability in aqueous environment, rapid blood clearance and low quantum yield [11, 13], which greatly limits its application in fluorescence imaging and photodynamic therapy. Meanwhile, a wide variety of gold nanoparticles including nanorods, nanotriangular particles, and nanostars have been applied in numerous PTT-based tumor treatments because of their strong and tunable surface plasmon resonance (SPR) effect and good biocompatibility [9-10, 14-16]. With a high absorption-to-scattering ratio in the NIR region, much more "hotspots" in the branch tips and multiple sharp edges favorable for generation heat, gold nanostars (GNS) are emerging rapidly not only as an optimal photothermal conversion material but also as a potential drug carrier [17-18]. Nevertheless, before their application into photo-based tumor therapy, it is of great importance to find the best way to fully exert the synergetic advantages of all these NIR-featured materials.

Recently PDT/PTT combination therapy has been developed as a promising joint therapy strategy to obtain a high therapeutic index. The combination of ICG with GNS represents a prospective option to achieve this coordinated NIR-based PDT/PTT. However, it must be acknowledged that previous work tended to load photosensitizers directly on the gold nanoparticles by either physical absorption or chemical bonding between the two elements [6, 14, 19-21]. Most of the physically absorbed drugs for PDT are immediately released from nanoparticles for PTT as soon as the drug-nanoparticle complex enters the body. Thereby, a large proportion of drug cannot reach the required treatment site, greatly reducing the therapeutic effect. On the other hand, the intrinsic fluorescence of the chemically bonded photosensitizer could suffer a drastic quenching effect from the gold nanoparticles because of the fluorescence resonance energy transfer (FRET) phenomenon [22-23], which brings great difficulties in tumor imaging and drug tracing. Therefore, a novel method to load photosensitizers on gold nanoparticles is needed for the effective performance of PDT/PTT combination therapy and the synchronous imaging.

Controlled drug release is the main task for photosensitizer-GNS complex in PDT/PTT combination therapy. Different stimulus including pH, light and temperature have been used in drug release to prevent its inactivity and minimize the side-effects to healthy tissues [1, 24-25]. Of those, the most appealing way in anti-cancer therapy is the use of the acidic environment of the tumor region to trigger the release of the drug due to pH variation. As a well-known building material for natural hard tissues such as bones and teeth with biocompatibility and nontoxicity, $CaCO_3$ is extensively utilized as drug carrier and biomedicine [26-27]. More importantly, $CaCO_3$ is stable at physiological pH of 7.4, while readily dissolved into bio-components of Ca^{2+} and CO_2 gas in response to an acidic environment [25]. Due to hypoxia and imperfect blood vessels system in the tumor tissue, the tumor cells form and maintain the extracellular acidic microenvironment by abnormal energy metabolism and the regulation of specific proteins. Take this as an opportunity, $CaCO_3$ was previously used as a cap to seal the encapsulated drug in the delivery device [25].

In this work, the NIR dye ICG was incorporated by the $CaCO_3$ coating of GNS with a characteristic NIR absorption to establish an elaborately designed nano-platform of GNS@$CaCO_3$/ICG which coordinated photothermal/photodynamic therapy in the NIR region (Scheme 1). We hypothesize that the ICG will form stable aggregates after being entrapped into the $CaCO_3$ layer which acted as an effective protecting agent to prevent ICG from degradation and rapid blood clearance [28]. The subsequent release of ICG was initiated by an effective displacement reaction in the presence of protons (H^+). When the nano-platform was exposed to tumor tissues characteristic of an acidic environment, the $CaCO_3$ layer immediately degraded and released the entrapped ICG, smartly converting the pH-triggered drug release into a tumor-triggered process. We observe the properties of GNS@$CaCO_3$/ICG, and monitor the biodistribution and excretion pathway base on its distinct NIR fluorescence, two-photon fluorescence and photoacoustic signal. As anticipated, the PA imaging together with fluorescence imaging clearly proved that GNS@$CaCO_3$/ICG had a great ability for tumor-specific and tumor-triggered drug release. And more, the remarkable antitumor efficacy of GNS@$CaCO_3$/ICG was demonstrated both *in vitro* and *in vivo* when subjected to 808 nm laser irradiation.
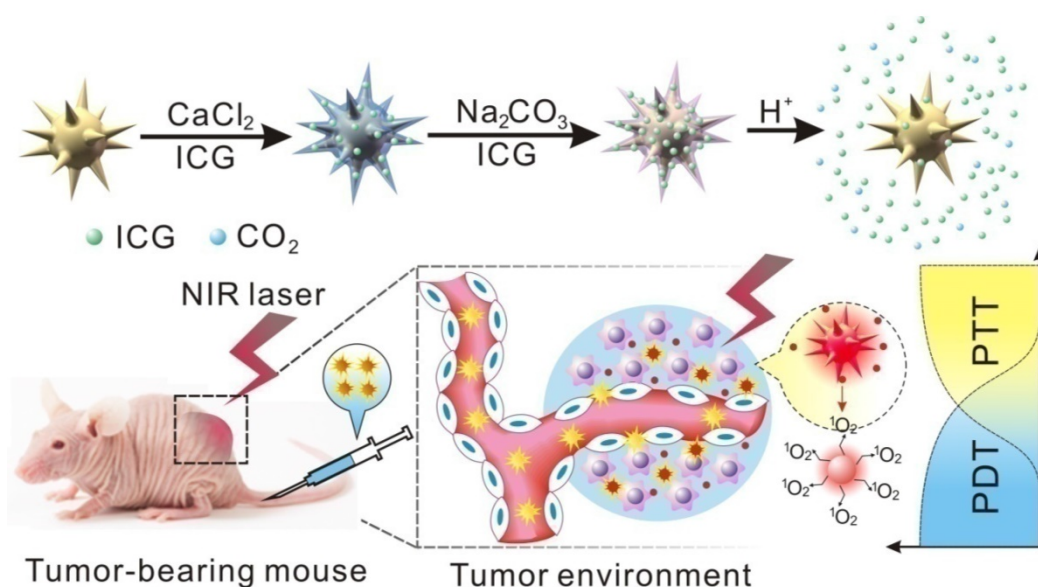
Scheme 1. Schematic illustration of construction and release mechanism of pH-trigger release system.

Materials and Methods

Materials

Gold (III) chloride trihydrate (HAuCl4·3H₂O, 99 %), trisodium citrate, hydrochloric acid, ascorbic acid, silver nitrate, calcium chloride and sodium carbonate were obtained from Sinopharm Chemical Reagent Co., Ltd. (Shanghai, China). Indocyanine green (ICG) was purchased from Sigma-Aldrich (St. Louis, USA). MGC803 cells were available in the Cell Bank of Type Culture Collection of Chinese Academy of Sciences. Cell culture products and reagent were purchased from GIBCO. Cell Counting Kit-8 (CCK-8) was purchased from Dojindo Molecular Technologies (Janpan). Deionized water (Millipore® Co., USA) with resistivity of 18.2 MΩ was used in all of the experiments.

Synthesis of GNS@CaCO₃/ICG

In a typical synthesis, the citrate gold seeds solution was prepared by adding 15 mL of 1 % trisodium citrate solution to 100 mL of boiling 1.0 mM HAuCl₄ solution under vigorous string for 15 minutes. Then, the solution was cooled and filtered using a 0.22 μm nitrocellulose membrane. 1 mL of cooled gold seed solution was added to 102 mL of HAuCl₄ (1.6 mM) containing HCl (1 mL, 1 M) under moderate stirring. Subsequently, freshly prepared AgNO₃ (1 mL, 3 M) and ascorbic acid (0.5 mL, 1 M), were added into the above mixture under moderate stirring. After that, 10 μL of 100 mM HS-PEG-COOH (Mw: 5000 Da) was added when the color of the reaction solution turned from light red to greenish-black. The reaction solution was kept under moderate stirring for 2 hours and GNS were acquired then. Next, calcium carbonate coating on GNSs was carried out according to Zhao's method with some modifications [25]. Briefly, 1 mL of CaCl₂ (10 mg/mL) and 20 μL of ICG (500 μg/mL) were added to 50 mL as-prepared GNSs followed by moderate stirring for 24 hours. And then, the acquired mixture was centrifuged to collect the particles and washed twice using deionized water (8500 × g, 10 min). After that, the precipitate was redispersed in 20 mL deionized water, 1 mL of Na₂CO₃ (10 mg/mL) and 20 μL of ICG (500 μg/mL) were added, and the mixture was kept under moderate stirring for 24 hours. The particles after centrifugation were then collected and stored at 4 ℃ for further use. In addition, GNS@ICG was obtained by simply sonication of a mixture of GNS and ICG for 15 min in an ice bath, and the GNS@ICG nanoparticles were washed three times with deionized water by centrifuging (9000 rpm, 8 min). Finally, all the products were stored at 4℃ for further use.

Characterization

The size, morphology and EDS (Energy-dispersive X-ray spectroscopy) elemental mapping of nanoparticles were characterized by TEM on a JEM-2100F (JEOL, Japan). The UV/vis absorption spectra of free ICG, GNSs and GNS@CaCO₃/ICG solution were recorded on a Varian Cary 50 spectrophotometer (Varian Inc., Palo Alto, CA, USA). Dynamic light scattering (DLS) and zeta potential of the specimens were completed using a NICOMP 380 ZLS Zeta Potential/Particle sizer (PSS Nicomp, Santa Barbara, CA, USA).

Profile of drug loading and release at different pH

In the drug loading experiment, the as-synthesized GNS@CaCO$_3$/ICG was collected by centrifugation at 8,800 rpm for 10 min and washed three times with deionized water to remove the physically adsorbed ICG. The amount of loaded drug in GNS@CaCO$_3$/ICG was determined by a UV-Vis spectrophotometer at 785 nm. The drug loading content and entrapment efficiency were calculated by the following equation: Drug loading (%) = (Weight of drug loaded) / (Weight of drug loaded and carriers) × 100%. Meanwhile, the drug release experiment of GNS@CaCO$_3$/ICG was performed at varying pH values. 2 mg GNS@CaCO$_3$/ICG was dispersed in 1 mL deionized water at different pH of 6.4 and 7.4. And then, GNS@CaCO$_3$/ICG solution (1 mL, 2 mg/mL) was transferred into a dialysis membrane (MWCO 3500) and immersed into 50 mL of the corresponding deionized water followed by continuous shaking (100 rpm) at 37 °C. At the pre-determined time intervals (0, 6, 12, 24, 36, 48, 60, 72, 84 h), 1 mL of release media was removed for UV-vis measurement and replenished with an equal volume of fresh media. As state above, the drug release experiment of GNS@CaCO$_3$/ICG was performed in serum-containing medium. Additionally, the fluorescent images of the released ICG (excitation: 710 nm; emission: 790 nm; integration time: 60 s) in storage solution specimen were acquired on Bruker In-Vivo FPRO imaging system (Billerica MA, USA). All the images were captured at the same parameter settings.

Singlet oxygen detection

The singlet oxygen sensor green (SOSG) regent was highly selective for $^1O_2$, which was employed here for the detection experiment. In our study, SOSG under the concentration of $2.5×10^{-6}$ M was introduced to measure the generation of $^1O_2$ from free ICG (20 µg/mL) and GNS@CaCO$_3$/ICG (equivalent 20 µg/mL ICG). The generated $^1O_2$ was determined by measuring recovered SOSG fluorescence (excitation = 494 nm).

Photothermal effects

The aqueous solutions of free ICG (20 µg/mL), GNS and GNS@CaCO$_3$/ICG (Equivalent 20 µg/mL ICG) were irradiated with a 808 nm laser at a power density of 1 W/cm^2 for 10min. The temperature of solutions was monitored every minute using an infrared thermal imaging camera.

Cell culture and CCK-8 assay

Gastric cancer is the third most common cause of cancer-related death in the world, and it remains difficult to cure. Therefore, human gastric cancer cell lines of MGC803 was choose for in vivo and in vitro experiment in this work. The MGC803 cells were cultured at 37 °C (5 % CO$_2$) in Dulbecco's modified Eagle's medium (DMEM, HyClone) supplemented with 10% fetal bovine serum (Gibco). CCK-8 assay was performed to investigate the cytotoxicity of the nano-platform. In brief, MGC803 cells were plated at a density of $1×10^4$ cells per well on 96-well plate. After 24 h incubation, the medium was replaced with fresh medium, and a series concentration of free ICG (0-30 µg/mL), GNSs and GNS@CaCO$_3$/ICG (Equivalent ICG 0-30 µg/mL) were added to the medium and incubated at 37 °C for 24 h, respectively. After that, the MGC803 cells were rinsed with PBS twice, and the cell viability was assessed by the CCK-8 assay.

Proliferation and viability assay

The MGC803 cell proliferation and viability were monitored by using Real-Time Cell Analyzer (RTCA Analyzer, Roche®). MGC803 cells were plated at a density of $1×10^4$ cells per well on 96-well plate. After 24 h incubation, the medium was replaced with fresh medium, and then the MGC803 cells were treated with PBS, GNSs and GNS@CaCO$_3$/ICG (equivalent 20 µg/mL ICG). After that, the electronic impedance across microelectrodes integrated into the bottom of cell culture E-Plates was captured every 5 minutes and the curves of Time-Normalized cell index were plotted by RTCA software (Roche®).

Cellular uptake assay

The two-photon luminescence of GNS and the NIR fluorescence of ICG were used to observe the cellular uptake of GNS@CaCO$_3$/ICG. In brief, MGC803 cells were incubated with GNS, ICG (20 µg/mL) and GNS@CaCO$_3$/ICG (equivalent 20 µg/mL ICG) for 12 h, and then they were washed three times with PBS to remove the unloaded nanoparticles followed by the replacing of complete culture medium. Finally, Two-photon luminescence images of GNS were obtained using a two-photon fluorescent microscope (Olympus FV 100, Janpan) with excitation at 780 nm and emission at 601-657 nm. Fluorescence images of cellular ICG were acquired with a confocal fluorescence microscope (Lecia SP8 STED 3X, Germany) with an excitation wavelength of 633 nm.

In Vitro thermal effect of GNS@CaCO$_3$/ICG

MGC803 cells were incubated with free ICG (20 µg/mL), GNSs and GNS@CaCO$_3$/ICG (equivalent ICG 20 µg/mL) for 24 h, and were carefully rinsed three times with PBS. And then, the MGC803 cells were irradiated by NIR laser at 808 nm with a power

of 1 W/cm^2 for 6 min. After that, the MGC803 cells were further incubated with fresh medium for 6 h, and then they were identified by calein AM live solution staining [29]. In addition, differences in metabolic activity of MGC803 cells treated with NIR irradiation were assessed by the CCK-8 assay.

Animal and tumor model

Female or male BALB/c athymic nude mice, 6-8 weeks of age and weighting 18-22 g were purchased from Shanghai LAC Laboratory Animal Co. Ltd., and housed in a SPF grade animal center. The use of all mice in this study complied with the current ethical considerations: Approval of institutional Animal Care and Use Committee of Shanghai Jiao Tong University. The mice were anesthetized by isoflurane, and 2×10^6 MGC803 cells suspended in 50µL saline were transplanted subcutaneously into the mice. And then all the mice were housed in animal center until the tumor size reached ≈ 150 mm^3.

In Vivo fluorescence imaging

Nude mice with MGC803 tumors were injected by a lateral tail vein with free ICG (1 mg kg^{-1}), GNS@ICG and GNS@CaCO$_3$/ICG (equivalent ICG 1 mg kg^{-1}). Time-course NIR fluorescent images of ICG (excitation: 710 nm; emission: 790 nm; integration time: 60 s) in mice after the injection were recorded via a Bruker *In-Vivo* FPRO imaging system (Billerica MA, USA). All the post-injection images were acquired with the same parameter settings. In order to further assess the bio-distribution of GNS@CaCO$_3$/ICG, these tumor-bearing mice were sacrificed at 72 h post-injection. Then the separated main organs and tumors were imaged at the same parameters as the above experiment.

Photoacoustic imaging

Nude mice were implanted with MGC803 cells in the back. When the tumors size reached ≈ 150 mm^3, photoacoustic imaging of tumors was implemented by Endra Nexus 128 PA scanner (Ann tbor, MI). Briefly, the mice were randomized into three groups of 4 animals per group, and intravenously injected with PBS, GNSs and GNS@CaCO$_3$/ICG (with the same elemental Au concentration, equivalent ICG 1 mg kg^{-1}) followed by placing in the protruding tip of the bowl. The images of the tumor site were consistently kept to facilitate the comparison. PA imaging of the tumor site exposed to the 808 nm irradiation by NIR laser was acquired according to different injection times (0, 4, 12, 24, 48 h). Reconstruction of single wavelength PA images was achieved by Osirix imaging software by displaying with transverse maximum intensity projection and an UCLA modality.

Antitumor efficacy of GNS@CaCO$_3$/ICG *In Vivo*

In vivo PDT/PTT combination therapy was performed using MGC803 tumor-bearing mice. The nude mice were randomized into four groups with 5 animals per groups, and they were intravenously injected with: (1) PBS, (2) free ICG (1 mg kg^{-1}), (3) GNS, (4) GNS@CaCO$_3$/ICG (equivalent ICG 1 mg kg^{-1}) in each group. The tumor region was irradiated with an 808 nm laser on the 2nd day after injection. To prevent the epidermis of tumor region from burning injury during the laser-treatment process, it was carried out for 6 min with 1 min interval after every 3 min of the exposure irradiated by the 808nm laser with a power density of 1.0 W/cm^2. Simultaneously, the temperature variation of the tumor site was monitored using an infrared thermal imaging camera. Tumor size was measured every four days by digital vernier caliper, and the whole experiment lasted 20 days since from the irradiation treatment. In the tumor growth monitoring experiments, the mice were sacrificed and the tumors were excised 20 days after the irradiation, and then the tumors were washed three times with PBS buffer for further investigation on hematoxylin & eosin (H & E) staining. The histo-pathological test was performed according to the standard laboratory procedures. After H & E staining, the sections were observed and photos were taken using an optical microscope (Olympus 1×71, Janpan).

Statistical analysis

Data were presented as mean ± SD unless otherwise stated. Statistical significance was determined using a two-tailed student's t-test. *P<0.05 was indicated to be statistically significant.

Results and discussion

Synthesis and characterization of GNS@CaCO$_3$/ICG

A layer-by-layer growth method was used to construct the multifunctional nano-probe GNS@CaCO$_3$/ICG. The surfactant-free GNSs were initially synthesized according to the seed-mediated template-assisted protocol with some modifications [30]. The acquired GNSs were subsequently covered by a layer of CaCO$_3$, into which ICG were simultaneously entrapped [25]. Transmission electron microscopy (TEM) images showed that the GNSs exhibited outstanding size uniformity with a diameter of 96 ± 7.5 nm, and dozens of branches extended from their surfaces (Figure 1A, Figure S1). After CaCO$_3$ precipitated on the surface of GNSs, the branches became shorter with GNS@CaCO$_3$/ICG appearing

more opaque (Figure 1B). These observations of $CaCO_3$ shell's growth were further confirmed by STEM, EDS (Energy-dispersive X-ray spectroscopy), and EDS elemental mapping images (Figure 1C, Figure S2). In addition, zeta potential of the nano-platform was recorded at pH 7.4. As shown in Figure S3 in Supporting Information, GNSs showed a negative zeta potential of -31.72 ± 2.36 mV due to the large amount of -COOH groups on the surface [31]. After covered by the $CaCO_3$ layer with a large amount of -OH groups [32], the nano-platform became less negative as -20.97 ± 1.56 mV, indicative of the successful precipitation of $CaCO_3$ on the GNS surface.

As shown in the UV/vis spectrum of gold nanostars (Figure 1D), GNSs had a strong longitudinal surface plasmon resonance wavelength (LSPRW) around 830 nm. After the $CaCO_3$ shell loaded with ICG precipitated on the GNSs' surface, the LSPRW of GNSs showed a blue-shift of ~40 nm to 790 nm, while the main peak of ICG which originally showed a maximum absorption at 785 nm and a shoulder at 710 nm in aqueous solution exhibited a red-shift to 890 nm in the nanoplatform $GNS@CaCO_3/ICG$ corresponding to the ICG molecule in the state of J-aggregate. With rising concentration, the ICG molecule readily forms dimers and oligomers, an absorption peak at 890 nm is due to J-aggregate formation [13]. It implied that ICG tended to form aggregates after being entrapped into the $CaCO_3$ layer of $GNS@CaCO_3$. In any case, these UV/vis extinction spectra showed the successful loading of ICG into the nano-platform. And the loading content of ICG in $GNS@CaCO_3/ICG$ was determined as 10.3 wt % by UV/vis spectra. Furthermore, the NIR fluorescence of ICG was weakened in $GNS@CaCO_3/ICG$ (Figure 1E), consistent with the fact that ICG molecules at higher concentration in water readily form dimmers and oligomers leading to a fluorescence decline [33]. This verified that ICG in $GNS@CaCO_3/ICG$ existed in aggregates giving little fluorescence. As a result, such characteristics of $GNS@CaCO_3/ICG$ favored the further formation of specific stimuli-triggered fluorescence signal.
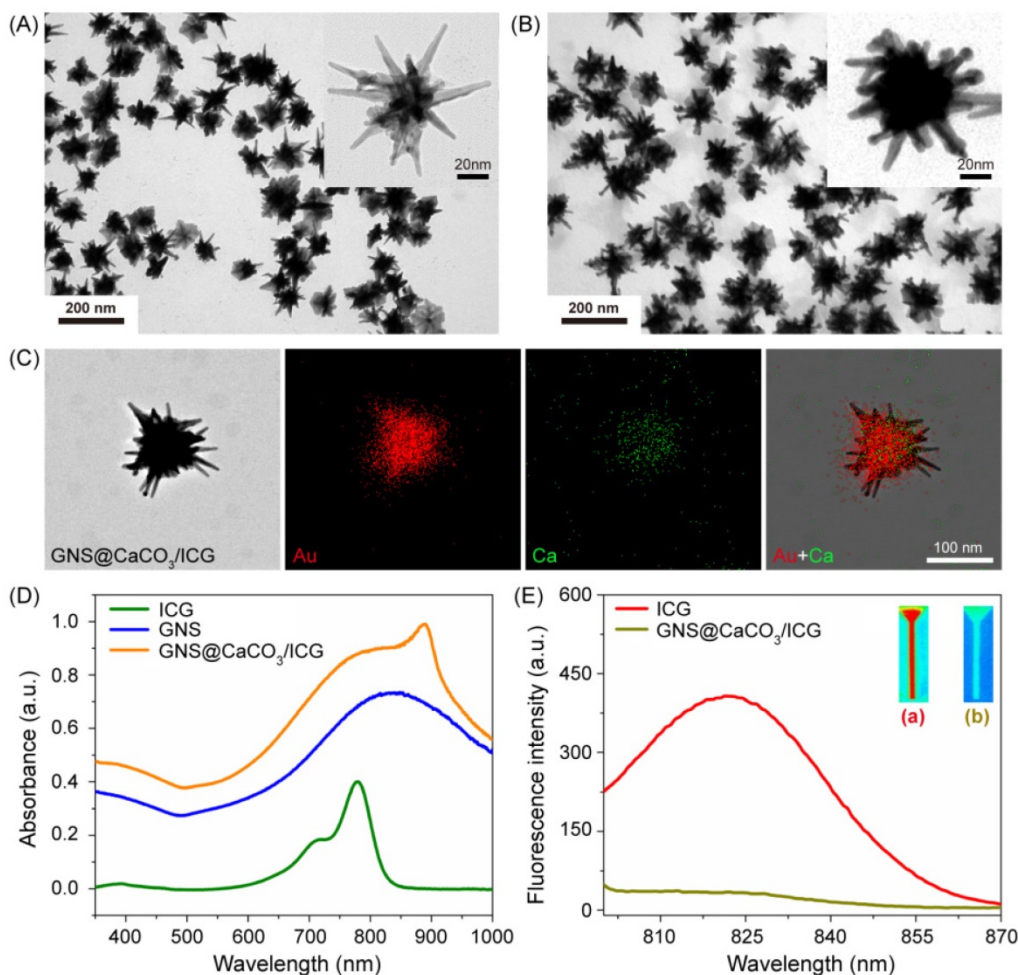
Figure 1. Characterization of GNS@CaCO₃/ICG. Transmission electron microscopy (TEM) images of GNS (A) and GNS@CaCO₃/ICG (B). (C) STEM and EDS elemental mapping images of GNS@CaCO₃/ICG. (D) Normalized UV-vis spectra of free ICG, GNS, GNS@PEG and GNS@CaCO₃/ICG. (E) Fluorescence spectra of free ICG and GNS@CaCO₃/ICG. The insert shows fluorescence images of free ICG (a) and GNS@CaCO₃/ICG (b). Excitation=710 nm.
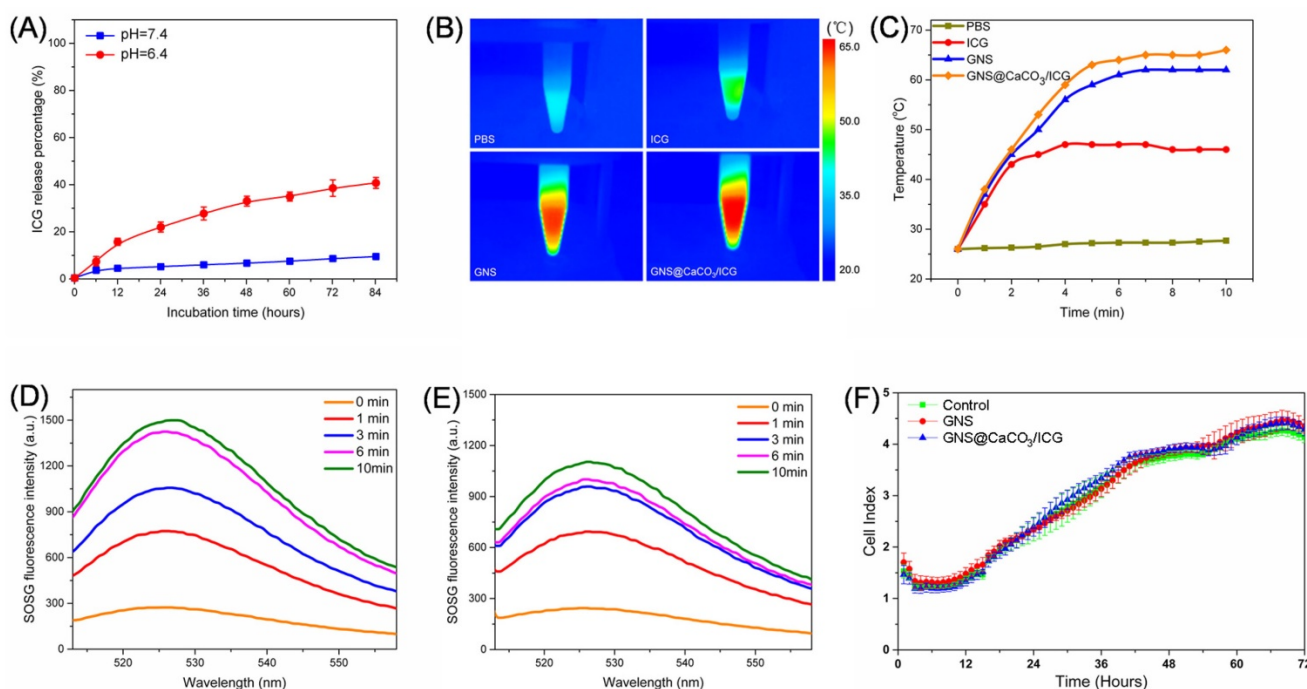
Figure 2. (A) Time course of ICG release from GNS@CaCO$_3$/ICG at different pH value (pH = 7.4, 6.4). (B) Thermal images of PBS, free ICG (20 µg/mL), GNS and GNS@CaCO$_3$/ICG (equivalent 20 µg/mL ICG) after 5 minutes of laser irradiation (808 nm, 1.0 W/cm^2). (C) Temperature change of photothermal effects of PBS, free ICG (20 µg/mL), GNS and GNS@CaCO$_3$/ICG (equivalent 20 µg/mL ICG) after laser irradiation (808 nm, 1.0 W/cm^2). (D) and (E) SOSG fluorescence spectra of free ICG (20 µg/mL) and GNS@CaCO$_3$/ICG (Equivalent ICG 20 µg/mL) after NIR laser irradiation (808 nm, 1.0 W/cm^2). (F) The effects of GNS (20 µg/mL) and GNS@CaCO$_3$/ICG (equivalent ICG 20 µg/mL) on MGC803 cells.

PH-triggered drug release

In order to investigate the pH-triggered release performance of ICG from GNS@CaCO$_3$/ICG, several drug release experiments were conducted at varying pH values. In principle, when GNS@CaCO$_3$/ICG encounters acidic environment, the CaCO$_3$ layer immediately degrades and releases the entrapped ICG. Meanwhile, CO$_2$ gas produced by the degradation may accelerate the process of drug release and assist their diffusion into monomers. As expected, a distinctive release of the entrapped ICG was triggered when the pH value was reduced to 6.4 (Figure 2A). In contrast, ICG release from GNS@CaCO$_3$/ICG dramatically decreased to no more than 10 % during the 72 h incubation period at pH 7.4 where CaCO$_3$ was unable to be decomposed. Similar results were clearly seen in the fluorescence images of the released-ICG from GNS@CaCO$_3$/ICG at different pH values (Figure S4). The more acidic the solution was (Ph 6.4), the more ICG GNS@CaCO$_3$/ICG would be released, and thus, the brighter the nano-platform could emit. Additionally, with the extension of incubation time, the NIR fluorescence became stronger and stronger. However, at physiological pH (7.4), the amount of ICG release from GNS without CaCO$_3$ layer was significantly higher than GNS@CaCO$_3$/ICG. ICG release from GNS/ICG was revealed to be 80 % during the 72 h incubation period

(Figure S5). In addition, the amount of ICG release from GNS@CaCO$_3$/ICG was very little (no more than 10 %) during the 84 h incubation period in serum-containing medium (Figure S6). All these observations clearly confirmed the highly effective pH-triggered drug release and the subsequent fluorescence generation behavior of GNS@CaCO$_3$/ICG.

Photodynamic/photothermal properties of GNS@CaCO$_3$/ICG

As the nano-platform was developed to be applied in PDT/PTT combination therapy, the photothermal and photodynamic effects of GNS@CaCO$_3$/ICG in aqueous solutions were initially measured. An aqueous solutions of free ICG (20 µg/mL), GNS and GNS@CaCO$_3$/ICG (Equivalent to 20 µg/mL ICG) were irradiated with an 808 nm laser in order to measure the photothermal effect. It was shown that the temperature between GNS and GNS@CaCO$_3$/ICG had no significant difference at each testing time point during the process of irradiation (Figure 2B and C), which suggested that the ability of GNS@CaCO$_3$/ICG and GNS to induct hyperthermia for PTT therapy is similar. As for the photodynamic effect, we investigated the capability to generate singlet oxygen from free ICG and GNS@CaCO$_3$/ICG under the NIR laser irradiation (808 nm). The singlet oxygen was quantitatively

determined by observing the fluorescence intensity change of singlet oxygen sensor green (SOSG) reagent excited at 494 nm, which is a specific singlet oxygen trap [8]. As Figure 2D and E showed, GNS@CaCO$_3$/ICG had almost the same capability to produce singlet oxygen as the free ICG. In addition, the experiments demonstrated that 6 min of NIR irradiation was enough for either photothermal or photodynamic effect. As a result, GNS@CaCO$_3$/ICG developed in this study possessed prospective photothermal and photodynamic qualities for further combination therapy.

In this study, to avoid potential cytotoxicity from cetyltrimethylammonium bromide (CTAB) we synthesized GNS according to the seed-mediated template-assisted method [34]. However, the biocompatibility of the nano-platform synthesized from the other two inorganic materials is not clear. In order to evaluate the effect of GNS@CaCO$_3$/ICG on the viability of MGC803 cell in detail, the cytotoxicity of GNS@CaCO$_3$/ICG was examined by CCK-8 assay and the cell proliferation was monitored by a Real-Time Cell Analyzer. As shown in Supporting Information Figure S7, after the 24 h incubation, GNS@CaCO$_3$/ICG showed no significant cytotoxicity in any of the concentrations tested. Similarly, there was no difference on the proliferation of cells between PBS groups and GNS@CaCO$_3$/ICG groups (Figure 2F). Moreover, GNS@CaCO$_3$/ICG showed no adverse effect on the cell proliferation rate as the incubation time extended. Therefore, GNS@CaCO$_3$/ICG exhibited excellent biocompatibility for further therapeutic application.

Cell uptake and localization of GNS@CaCO₃/ICG

Before performing the PTT/PDT combination therapy assay on MGC803 cells, the intracellular distribution of GNS@CaCO$_3$/ICG was observed based on the optical properties of GNS@CaCO$_3$/ICG for multimodal imaging. Because of the natural acidic environment inside endosomes/lysosomes and cytoplasm [35], the entrapped ICG was gradually released from GNS@CaCO$_3$/ICG, showing luminescence after endocytosis based on its pH-triggered fluorescence imaging. The NIR fluorescence imaging was performed in MGC803 cells incubated with free ICG (20 μg/mL) and GNS@CaCO$_3$/ICG (Equivalent to 20 μg/mL ICG). As shown in Figure 3A, both tested groups revealed prominent NIR fluorescence signals. However, the GNS@CaCO$_3$/ICG group showed a little stronger fluorescence owing to the pH-triggered ICG release (Figure S8), which demonstrates the prominent delivery and protection effect of our

GNS@CaCO$_3$/ICG on ICG. In addition, the prospective plasmon-enhanced two-photon luminescence of GNS core enabled an alternative assessment of the cellular uptake of GNS@CaCO$_3$/ICG compared with GNS [18, 36]. Two-photon luminescence microscopy showed an obvious luminescence all over the cytoplasm of MGC803 cells treated either with GNS@CaCO$_3$/ICG or GNS (Figure 3B), suggesting an efficient cellular uptake of our nanoparticles. Thus, both fluorescence imaging and two-photon microscopy validated the sufficient distribution of GNS@CaCO$_3$/ICG in cells.

PTT/PDT combination therapy of GNS@CaCO₃/ICG *In Vitro*

The good biocompatibility and wide distribution of the nano-platform in cells paved the way for the further use of GNS@CaCO$_3$/ICG-based PDT/PTT for killing MGC803 cells. MGC803 cells treated with free ICG (20 μg/mL), GNS or GNS@CaCO$_3$/ICG, all irradiated with an 808 nm laser were examined by both CCK-8 and dead-live staining assays. As expected, the nano-platform exhibited a distinct therapeutic effect via combined PTT/PDT treatment on the MGC-803 cells. As shown in Figure 3C, GNS@CaCO$_3$/ICG killed more cells than either free ICG or GNS after 6 min of NIR irradiation (1 W/cm^2), while no dead cells were observed in the PBS group. Consistent with the results of dead-live staining assay, the CCK-8 assay results showed that GNS@CaCO$_3$/ICG produced a higher anti-cancer effect than free ICG and GNS upon NIR irradiation (Figure 3D). These results indicated that GNS@CaCO$_3$/ICG produced a prominent therapeutic effect in cells via the combined PTT/PDT treatment upon NIR illumination, which was superior to the single PDT or PTT respectively mediated by free ICG or GNS.

Bio-distribution of GNS@CaCO₃/ICG *In Vivo*

Subsequently, the nano-platform of GNS@CaCO$_3$/ICG was applied in MGC803 tumor-bearing mice models. Nevertheless, before the PDT/PTT therapy, we conducted a fluorescence imaging assay based on the NIR fluorescence emitted by the ICG using tumor-bearing mice intravenously injected with free ICG, GNS@ICG and GNS@CaCO$_3$/ICG. As shown in Figure 4A, after the treatment with free ICG, the strong fluorescence was observed in the liver, indicating an enhanced liver accumulation. The fluorescence signal in the abdomen of the animals was observed after 6 h post-injection, due to ICG was excreted from the liver to the intestine. Over time, ICG gradually excreted from the liver, and no obvious fluorescence signal could be

detected 36 h post-injection probably because of the rapid blood clearance or the quenching effect from the internal environment. As for the GNS@ICG group, strong fluorescence signals were observed in liver just one hour after the intravenous injection as the physically absorbed ICG quickly released from GNS, while the weak signal in the tumor site was observed after 6 hours post-injection. In time, all the signals became weakened gradually. These results illustrated that a considerable amount of ICG had been released from GNS before reaching the tumor region. Therefore, this strategy would greatly affect the therapeutic effect.

On the other hand, in the GNS@CaCO$_3$/ICG group, weak fluorescence was observed in the tumor site just 1 hour after intravenous injection. After some time, the fluorescence signals of the tumor site gradually increased and reached a peak 24 h post-injection. These results indicated that a highly effective tumor-triggered drug release behavior of GNS@CaCO$_3$/ICG was occurring, strongly suggesting that the entrapped ICG was gradually being released from the GNS@CaCO$_3$/ICG platform as a result of the acidic environment of tumor regions which triggered the decomposition of the CaCO$_3$ layer. Moreover, it should be noted that the aggregate state for ICG in GNS@CaCO$_3$/ICG exhibit much higher stability than its monomers [13]. That is to say, the CaCO$_3$ shell in the nano-platform acted as an effective protecting agent to prevent ICG from degradation. In a nutshell, the whole nano-platform showed a prominent tumor-targeted fluorescence imaging capability by enhancing the stability of ICG in the circulation system and promoting the selective accumulation of ICG in the tumor region.
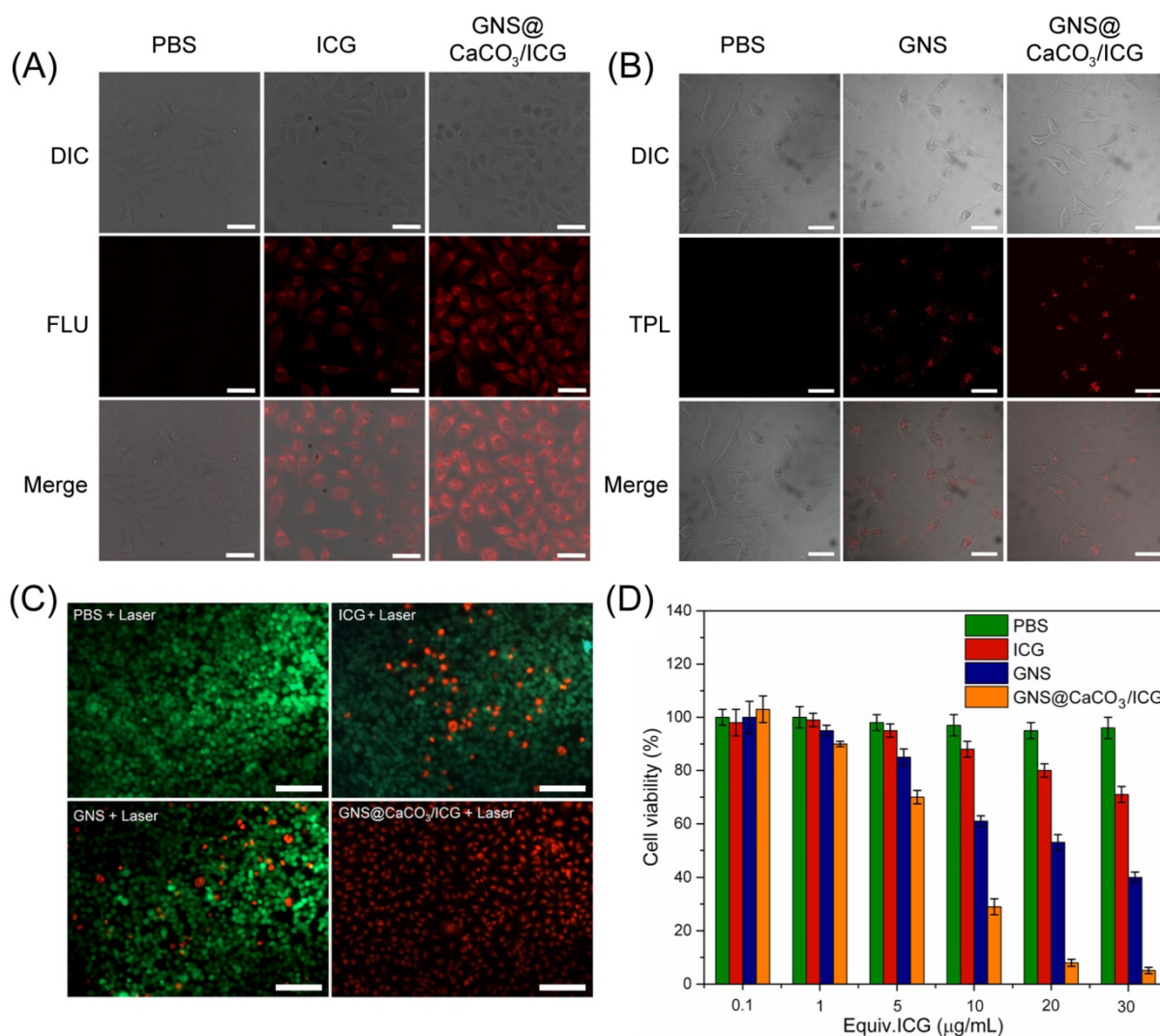
Figure 3. (A) Fluorescence images of ICG in MGC803 cells treated with free ICG and GNS@CaCO$_3$/ICG (excitation: 633 nm). Scare bars are 50 μm. (B) Two-photon laser scanning confocal microscopy images of GNS and GNS@CaCO$_3$/ICG in MGC803 cells (excitation=780 nm, emission= 601-657 nm). Scare bars are 100 μm. (C) Fluorescence images of Calcein AM/PI stained MGC-803 cells incubated with free ICG, GNS and GNS@CaCO$_3$/ICG respectively for 24 h after the irradiation of 808 nm laser (6 min, 1.0 W/cm^2). Scare bars are 200 μm. (D) Relative viability of MGC803 cells incubated with various concentrations of PBS, free ICG, GNS and GNS@CaCO$_3$/ICG after the irradiation of NIR laser (6 min, 1.0 W/cm^2), which was determined by CCK-8 assay.
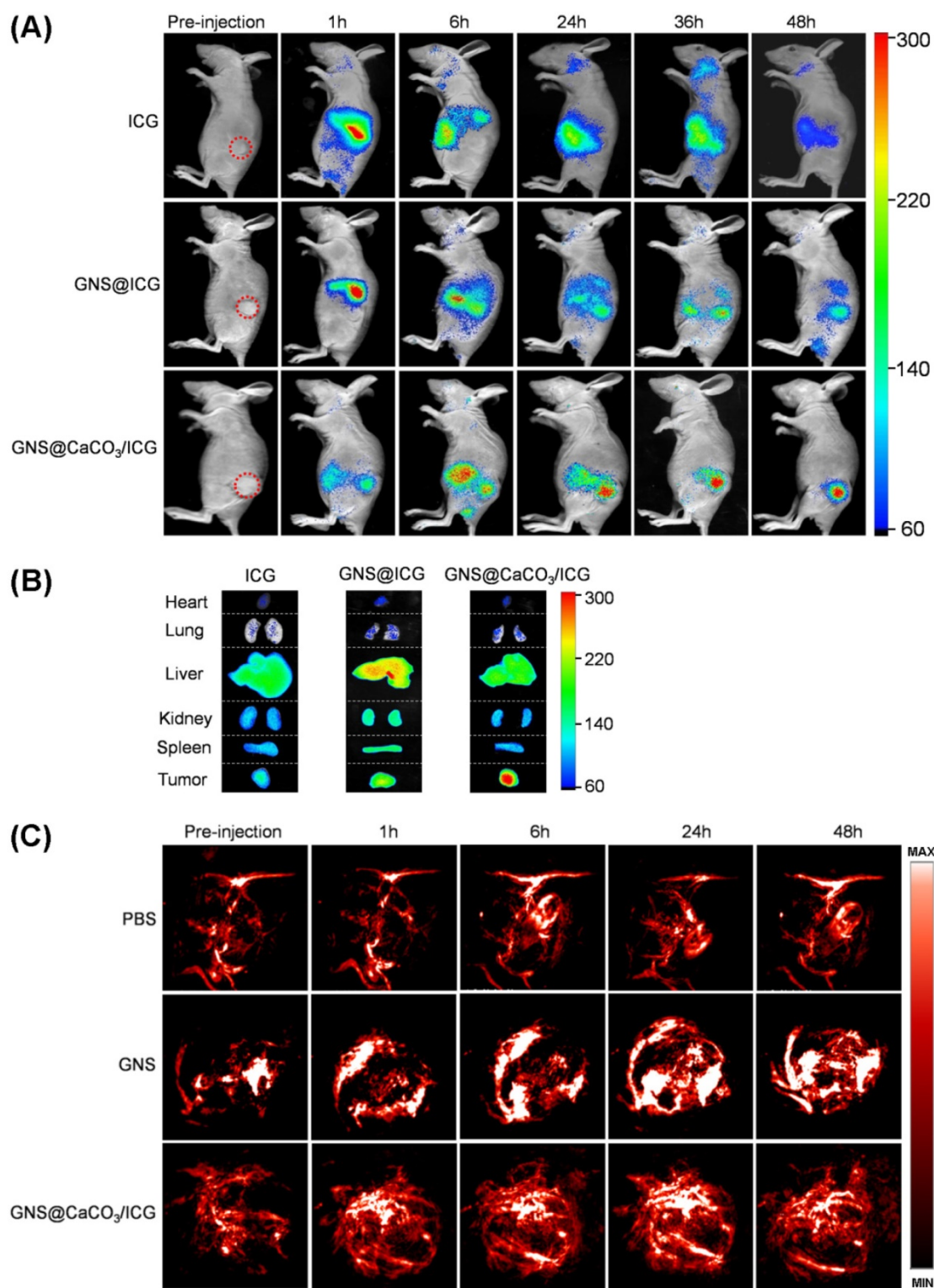
Figure 4. Distribution of GNS@CaCO₃/ICG in MGC803-tumor bearing mice. (A) Fluorescence images of MGC803 tumor-bearing mouse after intravenous injection of free ICG, GNS@ICG and GNS@CaCO₃/ICG over a period of 48 h (excitation: 710 nm; emission: 790 nm; integration time: 60 s). (B) Representative ex vivo fluorescence images of the main organs and tumors after intravenous injection of free ICG, GNS@ICG and GNS@CaCO₃/ICG (excitation: 710 nm; emission: 790 nm; integration time: 60 s). (C) Photoacoustic imaging of tumors: PA sequential images acquired before injection and after injection (1, 6, 24, 48 h) of PBS, GNS and GNS@CaCO₃/ICG (excitation: 810 nm).

Furthermore, the *ex vivo* fluorescence imaging of GNS@CaCO₃/ICG, GNS@ICG and ICG in the main organs 48 h after injection was conducted to provide additional insights into the bio-distribution and excretion pathway. Consistent with the results of the live animal imaging, GNS@CaCO₃/ICG injection

generated the strongest fluorescence signal in tumor compared to GNS@ICG and ICG (Figure 4B and figure S9). In addition, in the case of free ICG and GNS@ICG groups, most of the fluorescence signal was observed in the liver, while weak fluorescence was observed in the tumor tissues. Apparently, these results confirmed the highly effective tumor-triggered drug release behavior of GNS@CaCO$_3$/ICG, which was conducive to improve the therapeutic effect *in vivo*.

The Photoacoustic (PA) imaging relies on the photoacoustic effect which reflects conversion between laser and acoustic waves due to localized thermal excitation and absorption of electromagnetic. Therefore, PA imaging is recognized as an excellent technology to monitor the accumulation and distribution of metallic nanoparticles in tumor regions [6, 31]. In this study, the accumulation and distribution of GNS in tumors after the injection with GNS and GNS@CaCO$_3$/ICG were monitored in real-time using a PA scanner. The horizontal plane images of tumors vascularization were clearly seen as depicted in Figure 4C. For the GNS and GNS@CaCO$_3$/ICG groups, the PA signal from the intravascular system of the tumor became stronger 1 h post-injection compared to pro-injection. And as time passed, the PA signal was gradually stronger and reached a peak 24 h post-injection (Figure S10). However, for the PBS-treatment groups, the PA signal from the intravascular system of tumor showed no obvious changes all through the experiment. The PA signals of GNS@CaCO$_3$/ICG fitted its ICG fluorescence signals at each time point. The PA imaging together with fluorescence imaging clearly proved that GNS@CaCO$_3$/ICG had a great ability for tumor-specific and tumor-triggered drug release.

Combination antitumor efficacy of GNS@CaCO₃/ICG In Vivo

Based on the excellent tumor-triggered drug release behavior of GNS@CaCO$_3$/ICG, the nano-platform was finally exploited for anti-cancer efficacy on the MGC803 tumor-bearing mice. GNS are reported to have excellent photothermal conversion efficiency, increasing the temperature within a short laser-exposure time *in vitro*. However, the temperature produced by GNS, if not properly controlled, will induce irreversible damage to healthy tissues [37]. As described earlier in this paper, the NIR irradiation ensured that the temperature reached the threshold for thermo-therapy under the premise of keeping healthy tissues out of any excessive heat. Additionally, the 6 min irradiation time was adopted with 1min interval after every 3min of exposure so that the tumor temperature stayed under 45°C [38].

Upon irradiation with the 808 nm laser, the temperature variation of the tumor sites in the MGC803 tumor-bearing mice groups respectively injected with PBS, free ICG, GNS or GNS@CaCO$_3$/ICG was monitored using an infrared thermal imaging camera. As shown in Figure 5A, the tumor temperatures of GNS and GNS@CaCO$_3$/ICG groups were, respectively, 43.6 ^{o}C and 43.9 ^{o}C after 6 min irradiation (red circle in Figure 5A), while no significant temperature increase was observed in any other part of the anatomy of the mice. However, a moderate increase of temperature in the tumor sites, reaching 38.6 ^{o}C and 37.3 ^{o}C, was detected in mice respectively injected with free ICG and saline injected, which are insufficient to cause any damage [39-40]. In addition, the temperature quickly declined to its normal range just 1 min after removing the laser irradiation in all groups (Figure 5B). These results exhibited the specific hyperthermia of this nano-platform in tumor sites for *in vivo*.

The follow-up of the treated mice after the application of the combined PTT/PDT was further evaluated. As shown in Figure 5C and D, 20 days after the laser-irradiation treatment, there is a relatively rapid tumor growth in the saline groups and mice mortality rate in this group was the highest among all groups, indicating that simple laser irradiation without the help of reagents was ineffective to inhibit tumor growth. As expected, the average tumor size in the GNS@CaCO$_3$/ICG-injected groups was smaller than any other condition tested, including free ICG-injected group or GNS-injected group. Moreover, the GNS@CaCO$_3$/ICG group was the best one in terms of the survival rate among all the experimental groups. Consistent with the *in vitro* results, GNS@CaCO$_3$/ICG exhibited higher *in vivo* therapeutic effect than either GNS-based PTT or ICG-based PDT. Therefore, a strong combined effect of PTT/PDT in inhibiting tumor growth was established using GNS@CaCO$_3$/ICG platform under NIR irradiation.

In addition, to observe the deterioration of tumor cells after the coordinated PTT/PDT treatment, H&E staining of tumor sections collected from the treated mice was performed. As shown in Figure 5E, most tumor cells in the GNS@CaCO$_3$/ICG groups were destroyed, while in the GNS and ICG groups a small number of cell damage could be seen in the tumor region as indicated by the arrows. In contrast, there was no obvious tumor cell damage in the PBS group. As a result, from the pathological point of view, GNS@CaCO$_3$/ICG-based PDT/PTT was recognized as a highly effective strategy for tumor therapy.
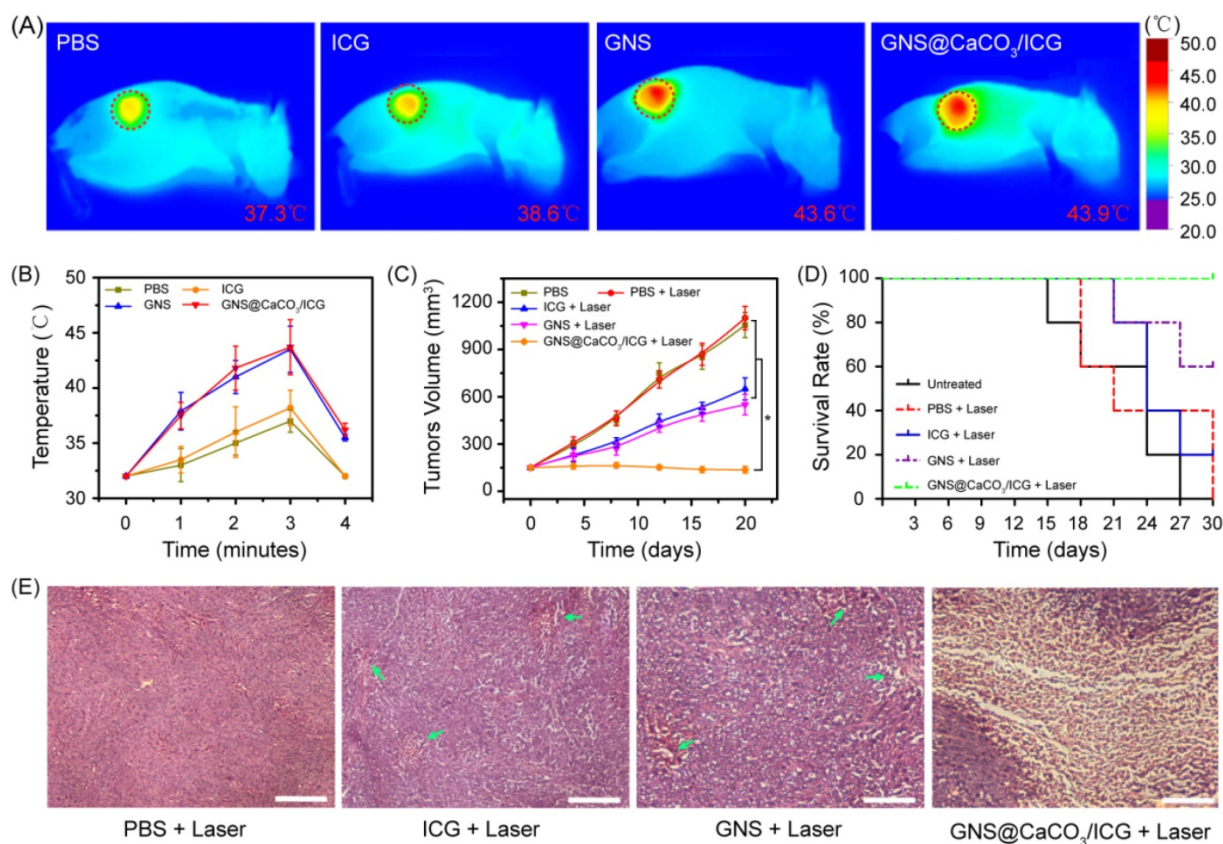
Figure 5. *In vivo* combination therapy of GNS@CaCO$_3$/ICG. (A) Infrared microscopic imaging of MGC803 tumor-bearing mouse on 2nd day post-injection of PBS, GNS and GNS@CaCO$_3$/ICG in the 808 nm laser irradiation process (1.0 W/cm^2). The red dashed circles highlighted the tumor regions. (B) Tumor temperature in various groups after laser irradiation. (C) Tumor volume in various groups after laser irradiation (n=5, *p<0.05). (D) Survival curves of MGC803 tumor-bearing mice after irradiation treatment. (E) Representative H&E sections of the tumor after combination therapy for 20 days. All scale bars are 200 µm.

Conclusions

In summary, we successfully constructed a novel tumor-triggered drug release nano-platform, GNS@CaCO$_3$/ICG, for effective photodynamic/ photothermal combination anti-cancer therapy upon 808 nm laser irradiation. In this nano-platform, calcium carbonate was introduced not only as a drug keeper to entrap ICG on the surface of GNS in the form of a stable aggregate, but also as the pH-responder to achieve a highly effective pH-triggered drug release behavior in the tumor region, simultaneously allowing for drug loading, targeted delivery, controlled release and imaging in a single platform. The application of GNS@CaCO$_3$/ICG for *in vitro* and *in vivo* therapy achieved the combined antitumor effects upon NIR irradiation, which surpassed the results of single PDT or PTT. Meanwhile, the distinct pH-triggered fluorescence imaging performance of GNS@CaCO$_3$/ICG implemented the tumor-targeted imaging and facilitated the observation of the drug bio-distribution in the tumor. Combined together, GNS@CaCO$_3$/ICG holds great promise for clinical all-in-one applications from tumor imaging or drug tracing to anti-tumor therapy.

Supplementary Material

Supplementary figures.
http://www.thno.org/v07p1650s1.pdf

Acknowledgements

Competing Interests

The authors have declared that no competing interest exists.

References

1. Zhang Z, Wang J, Nie X, Wen T, Ji Y, Wu X, et al. Near infrared laser-induced targeted cancer therapy using thermoresponsive polymer encapsulated gold nanorods. J Am Chem Soc. 2014; 136: 7317-26.
2. Cobley CM, Chen J, Cho EC, Wang LV. Xia Y. Gold nanostructures: a class of multifunctional materials for biomedical applications. Chem Soc Rev. 2011; 40: 44-56.

3. Huang P, Bao L, Zhang C, Lin J, Luo T, Yang D, et al. Folic acid-conjugated silica-modified gold nanorods for X-ray/CT imaging-guided dual-mode radiation and photo-thermal therapy. Biomaterials. 2011; 32: 9796-809.
4. Zhang Z, Wang L, Wang J, Jiang X, Li X, Hu Z, et al. Mesoporous silica-coated gold nanorods as a light-mediated multifunctional theranostic platform for cancer treatment. Adv Mater. 2012; 24: 1418-23.
5. Wang L, Lin X, Wang J, Hu Z, Ji Y, Hou S, et al. Novel insights into combating cancer chemotherapy resistance using a plasmonic nanocarrier: enhancing drug sensitiveness and accumulation simultaneously with localized mild photothermal stimulus of femtosecond pulsed laser. Adv Funct Mater. 2014; 24: 4229-39.
6. Li Y, Wen T, Zhao R, Liu X, Ji T, Wang H, et al. Localized electric field of plasmonic nanoplatform enhanced photodynamic tumor therapy. ACS Nano. 2014; 8: 11529-42.
7. Castano AP, Mroz P. Hamblin MR. Photodynamic therapy and anti-tumour immunity. Nat Rev Cancer. 2006; 6: 535-45.
8. Zhang C, Li C, Liu Y, Zhang J, Bao C, Liang S, et al. Gold nanoclusters-based nanoprobes for simultaneous fluorescence imaging and targeted photodynamic therapy with superior penetration and retention behavior in tumors. Adv Funct Mater. 2015; 25: 1314-25.
9. Wang Y, Black KC, Luehmann H, Li W, Zhang Y, Cai X, et al. Comparison study of gold nanohexapods, nanorods, and nanocages for photothermal cancer treatment. ACS Nano. 2013; 7: 2068-77.
10. Schnarr K, Mooney R, Weng Y, Zhao D, Garcia E, Armstrong B, et al. Gold nanoparticle-loaded neural stem cells for photothermal ablation of cancer. Adv Healthc Mater. 2013; 2: 976-82.
11. Luo S, Zhang E, Su Y, Cheng T. Shi C. A review of NIR dyes in cancer targeting and imaging. Biomaterials. 2011; 32: 7127-38.
12. Zheng C, Zheng M, Ping G, Jia D, Zhang P, Shi B, et al. Indocyanine green-loaded biodegradable tumor targeting nanoprobes for invitro and invivo imaging. Biomaterials. 2012; 33: 5603-9.
13. Holzer W, Mauerer M, Penzkofer A, Szeimies RM, Abels C, Landthaler M, et al. Photostability and thermal stability of indocyanine green. J Photochem Photobiol B: Biol. 1998; 47: 155-64.
14. Xiao Y, Hong H, Matson VZ, Javadi A, Xu W, Yang Y, et al. Gold nanorods conjugated with Doxorubicin and cRGD for combined anticancer drug delivery and PET imaging. Theranostics. 2012; 2: 757-68.
15. Nie L, Wang S, Wang X, Rong P, Ma Y, Liu G, et al. In vivo volumetric photoacoustic molecular angiography and therapeutic monitoring with targeted plasmonic nanostars. Small. 2014; 10: 1585-93.
16. Cho EC, Camargo PH. Xia Y. Synthesis and characterization of noble-metal nanostructures containing gold nanorods in the center. Adv Mater. 2010; 22: 744-8.
17. Yuan H, Liu Y, Fales AM, Li YL, Liu J. Vo-Dinh T. Quantitative surface-enhanced resonant Raman scattering multiplexing of biocompatible gold nanostars for in vitro and ex vivo detection. Anal Chem. 2013; 85: 208-12.
18. Yuan H, Fales AM. Vodinh T. TAT peptide-functionalized gold nanostars: enhanced intracellular delivery and efficient NIR photothermal therapy using ultralow irradiance. J Am Chem Soc. 2012; 134: 11358-61.
19. Wang S, Huang P, Nie L, Xing R, Liu D, Wang Z, et al. Single continuous wave laser induced photodynamic/plasmonic photothermal therapy using photosensitizer-functionalized gold nanostars. Adv Mater. 2013; 25: 3055-61.
20. Topete A, Alatorre-Meda M, Iglesias P, Villar-Alvarez EM, Barbosa S, Costoya JA, et al. Fluorescent drug-loaded, polymeric-based, branched gold nanoshells for localized multimodal therapy and imaging of tumoral cells. ACS Nano. 2014; 8: 2725-38.
21. Jang B. Choi Y. Photosensitizer-conjugated gold nanorods for enzyme-activatable fluorescence imaging and photodynamic therapy. Theranostics. 2012; 2: 190-7.
22. Dulkeith E, Ringler M, Klar TA, Feldmann J, Muñoz JA. Parak WJ. Gold nanoparticles quench fluorescence by phase induced radiative rate suppression. Nano Lett. 2005; 5: 585-9.
23. Quach AD, Georgeta C, Tarr MA. Zeev R. Gold nanoparticle-quantum dot-polystyrene microspheres as fluorescence resonance energy transfer probes for bioassays. J Am Chem Soc. 2011; 133: 2028-30.
24. Huang P, Lin J, Wang X, Wang Z, Zhang C, He M, et al. Light-triggered theranostics based on photosensitizer-conjugated carbon dots for simultaneous enhanced-fluorescence imaging and photodynamic therapy. Adv Mater. 2012; 24: 5104-10.
25. Zhao X, Yuan Z, Yildirimer L, Zhao J, Lin ZY, Cao Z, et al. Tumor-triggered controlled drug release from electrospun fibers using inorganic caps for inhibiting cancer relapse. Small. 2015; 11: 4284-91.
26. Wei J, Cheang T, Tang B, Xia H, Xing Z, Chen Z, et al. The inhibition of human bladder cancer growth by calcium carbonate/CaIP6 nanocomposite particles delivering AIB1 siRNA. Biomaterials. 2013; 34: 1246-54.
27. Xu AW, Yu Q, Dong WF, Antonietti M. Cölfen H. Stable amorphous $CaCO_3$ microparticles with hollow spherical superstructures stabilized by phytic acid. Adv Mater. 2005; 17: 2217-21.
28. Lee CH, Cheng SH, Wang YJ, Chen YC, Chen NT, Souris J, et al. Near-infrared mesoporous silica nanoparticles for optical imaging: Characterization and in vivo biodistribution. Adv Funct Mater. 2009; 19: 215-22.
29. Zheng M, Zhao P, Luo Z, Gong P, Zheng C, Zhang P, et al. Robust ICG theranostic nanoparticles for folate targeted cancer imaging and highly effective photothermal therapy. Acs Appl Mater Interfaces. 2014; 6: 6709-16.
30. Yuan H, Khoury CG, Hwang H, Wilson CM, Grant GA. Vo-Dinh T. Gold nanostars: surfactant-free synthesis, 3D modelling, and two-photon photoluminescence imaging. Nanotechnology. 2012; 23: 075102.
31. Liang S, Li C, Zhang C, Chen Y, Xu L, Bao C, et al. CD44v6 monoclonal antibody-conjugated gold nanostars for targeted photoacoustic imaging and plasmonic photothermal therapy of gastric cancer stem-like cells. Theranostics. 2015; 5: 970-84.
32. Guo Y, Zhou Y. Jia D. Fabrication of hydroxycarbonate apatite coatings with hierarchically porous structures. Acta Biomater. 2008; 4: 334-42.
33. Saxena V, Sadoqi M. Shao J. Degradation kinetics of indocyanine green in aqueous solution. Journal of Pharmaceutical Sciences. 2003; 92: 2090-7.
34. Lau IP, Chen H, Wang J, Ong HC, Leung KC, Ho HP, et al. In vitro effect of CTAB- and PEG-coated gold nanorods on the induction of eryptosis/erythroptosis in human erythrocytes. Nanotoxicology. 2012; 6: 847-56.
35. Zhao J, Liu J, Xu S, Zhou J, Han S, Deng L, et al. Graft copolymer nanoparticles with pH and peduction dual-induced disassemblable property for enhanced intracellular curcumin release. Acs Appl Mater Interfaces. 2013; 5: 13216-26.
36. Durr NJ, Larson T, Smith DK, Korgel BA, Sokolov K. Ben-Yakar A. Two-photon luminescence imaging of cancer cells using molecularly targeted gold nanorods. Nano Lett. 2007; 7: 941-5.
37. Song CW, Park HJ, Lee CK. Griffin R. Implications of increased tumor blood flow and oxygenation caused by mild temperature hyperthermia in tumor treatment. Int J Hyperthermia. 2005; 21: 761-7.
38. Zheng M, Yue C, Ma Y, Gong P, Zhao P, Zheng C, et al. Single-step assembly of DOX/ICG loaded lipid-polymer nanoparticles for highly effective chemo-photothermal combination therapy. ACS Nano. 2013; 7: 2056-67.
39. Hirsch L, Stafford R, Bankson J, Sershen S, Rivera B, Price R, et al. Nanoshell-mediated near-infrared thermal therapy of tumors under magnetic resonance guidance. Proc. Natl. Acad. Sci. 2003; 100: 13549-54.
40. Tang Y. Mcgoron AJ. Combined effects of laser-ICG photothermotherapy and doxorubicin chemotherapy on ovarian cancer cells. Journal of Photochemistry & Photobiology B Biology. 2009; 97: 138-44.